ADVANCED MATERIALS INTERFACES
www.advmatinterfaces.de

Indium Selenide/Indium Tin Oxide Hybrid Films for Solution-Processed Photoelectrochemical-Type Photodetectors in Aqueous Media

Gabriele Bianca, Marilena Isabella Zappia, Sebastiano Bellani, Michele Ghini, Nicola Curreli, Joka Buha, Valerio Galli, Mirko Prato, Aljoscha Soll, Zdeněk Sofer, Guglielmo Lanzani, Ilka Kriegel, and Francesco Bonaccorso**

2D metal monochalcogenides have recently attracted interest for photoelectrochemical (PEC) applications in aqueous electrolytes. Their optical bandgap in the visible and near-infrared spectral region is adequate for energy conversion and photodetection/sensing. Their large surface-to-volume ratio guarantees that the charge carriers are photogenerated at the material/electrolyte interface, where redox reactions occur, minimizing recombination processes. However, solution-processed photoelectrodes based on these materials exhibit energy conversion efficiencies that are far from the current state of the art expressed by established technologies. This work reports a systematic morphological, spectroscopic, and PEC characterization of solution-processed films of photoactive InSe flakes for PEC-type photodetectors. By optimizing the thickness and hybridizing InSe flakes with electrically conductive Sn:In_2O_3 (ITO) nanocrystals, photoanodes with a significant photoanodic response in both acidic and alkaline media are designed, reaching responsivity up to 60.0 mA W^{-1} (external quantum efficiency = 16.4%) at +0.4 V versus RHE under visible illumination. In addition, a strategy based on the use of sacrificial agents (i.e., 2-propanol and Na_2SO_3) is proposed to improve the stability of the InSe and ITO/InSe photodetectors. Our data confirm the potential of 2D InSe for PEC energy conversion and sensing applications, remarking the challenges related to InSe stability during anodic operation.

1. Introduction

The quest for new photo(electro)catalytic materials is an ever-expanding research field, potentially addressing the need for sustainable fuel and chemical production,[1] environmental remediation,[2] advanced analytical sensing systems,[3] as well as novel concept of self-powered (or low-voltage operating) photoelectrochemical (PEC)-type photodetectors.[4,5] Portable electrochemical workstations, combined with wireless data communication *apparati*, offer the possibility to miniaturize PEC-type photodetector systems for monitoring analytes (e.g., blood glucose) in liquid media[6] and underwater optical communication.[5] Compared to electrochemical devices, PEC-type photodetectors can probe either analytes or light intensity through photoinduced electrochemical reactions, enabling differential mode operation that reduces the background signal down to the limit of lock-in detection noise[7] and eliminating the need for recurrent recalibration procedures.[8]

In this context, 2D materials intrinsically represent an attractive class of

G. Bianca, F. Bonaccorso
Graphene Labs
Istituto Italiano di Tecnologia
via Morego 30, Genova 16163, Italy
G. Bianca
Dipartimento di Chimica e Chimica Industriale
Università degli Studi di Genova
via Dodecaneso 31, Genoa 16146, Italy

The ORCID identification number(s) for the author(s) of this article can be found under https://doi.org/10.1002/admi.202201635.

DOI: 10.1002/admi.202201635

M. I. Zappia, S. Bellani, V. Galli, F. Bonaccorso
Bonaccorso BDimensional S.p.A.
via Lungotorrente Secca 30R, Genova 16163, Italy
E-mail: s.bellani@bedimensional.it; f.bonaccorso@bedimensional.it
M. Ghini, N. Curreli, I. Kriegel
Functional Nanosystems
Istituto Italiano di Tecnologia
via Morego 30, Genova 16163, Italy
J. Buha
Nanochemistry
Istituto Italiano di Tecnologia
via Morego 30, Genova 16163, Italy
V. Galli, G. Lanzani
Dipartimento di Fisica
Politecnico di Milano
Piazza Leonardo da Vinci 32, Milano 20133, Italy

nanomaterials.[9–11] In fact, their large surface-to-volume ratio guarantees that the charge carriers are directly photogenerated at the material/electrolyte interface, in which redox reactions take place, thus limiting charge recombination processes.[9,10] Among 2D materials, graphene derivatives,[12] metal dichalcogenides,[13,14] metal monochalcogenides,[15–18] metal phosphotrichalcogenides,[19,20] black phosphorous,[21] graphitic carbon nitrides[22] and oxides[23] have been reported as water splitting photo(electro)catalyst under UV/visible illumination, as well as for photocatalytic/PEC nitrogen fixation[24] and CO_2 reduction,[25] demonstrating their potential for aqueous photocatalysis and PEC applications. Thus, 2D material-based PEC-type photodetectors, as well as other configurations based on photovoltaic effect as the working mechanism (e.g., vertical heterojunction photodiodes[26]), have the potential to operate at low-voltage or even in self-powered detection modes that are incompatible with traditional photodetectors based on the photoconductive effect (PCE).[3] In principle, they can also overcome the limits of PCE photodetectors,[27], e.g., limited response times[27] and the need for expensive and/or complex manufacturing methods for the fabrication of interdigitated electrodes and transfer of isolated flake as the photoactive component.[27] By properly engineering mesoporous photoelectrodes, 2D material-based PEC-type photodetectors promise to efficiently operate even at high illumination intensity (e.g., >10 mW cm^{-2}, including simulated AM 1.5G solar irradiation at 100 mW cm^{-2}), for which PCE photodetectors typically lose their performance.[28,29]

In this context, 2D indium selenide (InSe), exfoliated from its β polymorph bulk counterpart,[30] fulfills the fundamental requirements for water splitting photo(electro)catalysts,[17], i.e.,: 1) valence band (VB) maximum energy (E_{VBM}) lower than the reduction potential of O_2/H_2O ($E(O_2/H_2O)$); 2) conduction band (CB) minimum energy (E_{CBM}) higher than the reduction potential of H^+/H_2 ($E(H^+/H_2)$). In addition, pioneering studies demonstrated n-type field-effect transistors (FETs) based on 2D InSe, with electron mobility (μ_e) at room temperature on the order of 10^3 cm^2 V^{-1} s^{-1},[31,32] which is higher than those achieved by other high-mobility 2D semiconducting materials (metal dichalcogenides, e.g., MoS_2,[33] or elemental materials, such as black phosphorous[34]). The high carrier mobility of 2D InSe has been associated with the quantum Hall effect, for which the conduction electrons reside in a single 2D sub-band, having a small effective mass.[32,35] Lastly, the possibility to produce 2D materials (including 2D InSe) in form of inks through liquid-phase exfoliation (LPE) represents an obvious opportunity to simplify the fabrication of PEC photodetectors through high-throughput and cost-effective printing techniques.[36,37] By depositing 2D material inks, mesoporous structures can be simply fabricated, maximizing the photoactive material/electrolyte interface at which the redox reactions take place.[15,16,18] Despite the experimental progress and the theoretical promises, 2D InSe-based photo(electro)catalysts exhibit energy conversion efficiencies still far from the current state-of-the-art expressed by established technologies under hands-on illuminations (e.g., solar one).[38] In general, technical aspects related to the ultimate performance of such nanomaterial into practical photoelectrode configurations,[39] as well as in real photocatalytic reactors,[40] are still missing. In fact, experimental studies demonstrated solution-processed InSe-based PEC-type photodetectors with responsivities on the order of few μA W^{-1}, corresponding to external quantum efficiencies (EQEs) inferior to 10^{-2}%.[41] These EQE values are significantly below the theoretical limit of 100% (in absence of nontrivial multiple excitation generation).[42,43] Moreover, the responsivity of InSe-based PEC-type photodetectors lag behind the values reached by other solution-processed solid-state photodetectors (e.g., >1 A W^{-1}), which exploit photoconductive effect (PCE) to achieve EQE above 100%.[28,29,44] The performance limits of solution-processed 2D InSe-based photoelectrodes have been attributed to the high contact electrical resistance between InSe flakes,[18,28,29] hindering the realization of photoactive films that advantageously combine high optical light absorption and effective transport of the photogenerated charge toward the current collector.[45] Novel strategies are therefore needed to overcome the intrinsic limit of solution-processed 2D InSe-based photoactive films.

In this work, we rationalized that the construction of hybrid structures composed by 2D InSe flakes and transparent conductive oxide nanocrystals (NCs) can represent an effective approach to overwhelm the dichotomy between efficient light absorption and effective charge transport in solution-processed 2D material-based photoelectrodes. Thus, we design, produce, and characterize solution-processed hybrid photoelectrodes made of thin films of liquid-phase exfoliated single-/few-layer InSe flakes and Sn:In_2O_3 (ITO) NCs. Here, ITO NCs were used to electrically connect InSe flakes, providing efficient charge transport pathways in hybrid photoactive ITO/InSe films in PEC-type photodetectors.[46] Noteworthy, ITO NCs represent an example of plasmonic doped metal oxides nanocrystals, whose tunable optoelectronic properties (e.g., carrier densities ranging over several orders of magnitude –10^{24}–10^{27} m^{-3}),[47] have been widely exploited for a broad variety of applications, e.g., (bio)sensing,[48] multielectron transfer,[49] smart windows[50] and transparent conductive films.[51,52] Even more, ITO NCs have been coupled with other 2D materials to facilitate charge carrier separation at the interfaces of 0D/2D systems,[53,54] giving the opportunity to implement innovative solutions in the field of optoelectronics and energy conversion and storage.[46,55] To prove the effectiveness of the hybridization strategy, we carried out an in-depth morphological, structural, spectroscopic and PEC characterization of hybrid films, together with the ones of InSe and ITO NCs. To extend previous studies, which focused on the PEC properties of 2D InSe in alkaline media and reached responsivity in the order of μA cm^{-2},[41] we reveal that 2D InSe-based films show the highest photoanodic responses in acidic media (0.5 M H_2SO_4), reaching responsivities up to 31.1 mA W^{-1} (at +0.8 V

M. Prato
Materials Characterization Facility
Istituto Italiano di Tecnologia
via Morego 30, Genova 16163, Italy
A. Soll, Z. Sofer
Department of Inorganic Chemistry
University of Chemistry and Technology Prague
Technická 5, Prague 6 166 28, Czech Republic
G. Lanzani
Center for Nano Science and Technology @PoliMi
Istituto Italiano di Tecnologia
via Pascoli 70/3, Milano 20133, Italy

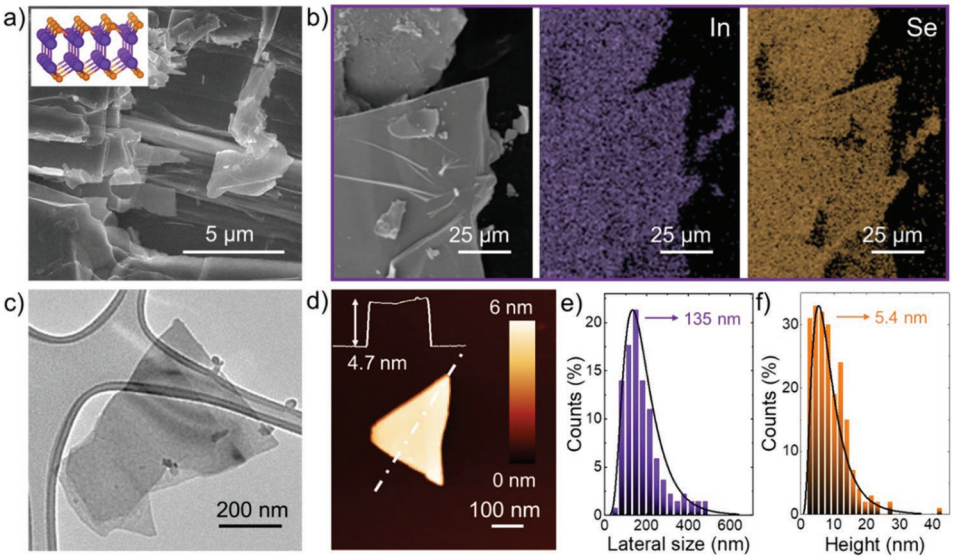

Figure 1. a) SEM image of fragments of β-InSe crystal, showing their layered edge structure. b) SEM image of fragments of β-InSe crystals and the corresponding EDS maps for In ($L\alpha = 3.286$ eV, violet) and Se ($L\alpha = 1.4$ eV, orange). c) BF-TEM image of the overlapped InSe flakes produced through LPE of InSe crystal in IPA. d) AFM image of a representative InSe few-layer flake, showing the height profile along the section indicated by the white dashed line. e) Statistical analysis of the lateral dimension of InSe flakes, as calculated from the analysis of the BF-TEM images. f) Statistical analysis of the thickness of InSe flakes, as calculated from the analysis of the AFM images.

vs reversible hydrogen electrode—RHE—under 0.5 mW cm^{-2} for 455 nm illumination wavelengths). By optimizing the InSe mass loading in the photoelectrodes and hybridizing the InSe flakes with ITO NCs, we increased the responsivity of the PEC photodetectors up to 60.0 mA W^{-1} (EQE 16.3%) at +0.4 V versus RHE under the same illumination condition. In addition, our analysis revealed a poor PEC stability of the InSe and ITO/InSe-based photoanodes in both acidic and alkaline media, indicating the need to implement adequate strategies for practical applications. The use of prototypical sacrificial agents, e.g., 2-propanol (IPA) and Na_2SO_3,[56,57] in the electrolytes was therefore considered to limit oxidation/corrosion of the photoactive materials. Although sacrificial agents improved the stability of the devices, the PEC properties degradation was blocked only in 1 M KOH and 0.35 M Na_2SO_3. Our data confirm the potential of 2D InSe for PEC energy conversion and sensing applications, while remarking on the current challenges related to their stability during anodic operation.

2. Results and Discussion

2.1. InSe Crystal Synthesis, Exfoliation, and Characterization

β-InSe crystal was synthesized through Bridgman-Stockbarger method,[58] which effectively avoids the concomitant growth of other InSe polymorphs, e.g., γ and ε material phases.[30] **Figure 1**a shows a representative scanning electrode microscopy (SEM) image of fragments of the InSe crystal, revealing their layered edge structures. The SEM-coupled with energy-dispersive X-ray spectroscopy (EDS) analysis (Figure 1b) evidenced an almost ideal elemental stoichiometry (In-to-Se atomic ratio ≈1.07, see Table S1, Supporting Information). Subsequently, β-InSe crystal was exfoliated through ultrasonication-assisted LPE in anhydrous IPA,[36,59,60] followed by sedimentation-based separation (SBS)[61,62] to remove unexfoliated crystals from the exfoliated material. The methods of synthesis, exfoliation, and characterization of InSe flakes are fully described in the Experimental Method section (Supporting Information). Even though ultrasonication-assisted LPE represents a lab-scale process with limited productivity, other LPE techniques, e.g., wet-jet milling exfoliation,[63] can replace the former to massively produce exfoliated materials for industrial applications,[64,65] preserving the material structural and chemical quality. The morphology of the exfoliated sample was evaluated through bright-field transmission electron microscopy (BF-TEM) and atomic force microscopy (AFM) measurements. Figure 1c shows a BF-TEM image of overlapped flakes, which exhibit non-regular shapes with straight edges. Figure 1d reports an AFM image of a quasi-triangular few-layer flake with a thickness of ≈4.7 nm (monolayer thickness of ≈0.84 nm).[66] The statistical analysis of the BF-TEM images (Figure 1e) indicates that lateral sizes of the flakes range from 50 to 710 nm, following a log-normal distribution peaked at ≈135 nm. Meanwhile, the statistical analysis of the AFM thickness (Figure 1f) shows that the exfoliated sample is mainly composed of few-layer InSe flakes, being the data fitted by a log-normal distribution peaked at 5.4 nm. As discussed hereafter, β-InSe shows a thickness-dependent bandgap that ranges from ≈1.2 eV for the bulk[67] to ≈2.1 eV for the monolayer at room temperature,[68] evolving from a direct to a pseudo-direct (weak indirect) semiconductor when the crystal thickness is reduced to less than six layers.[69]

Therefore, the abundance of few-layer flakes with a polydisperse thickness in our exfoliated sample is adequate for obtaining a photoactive material for PEC devices. In fact, the mixing of flakes with different thicknesses and optical bandgap results in nanoscale tandem systems that maximize the light energy absorption through photosynthetic-like processes.[16] The structural properties of the exfoliated samples were evaluated through X-ray diffraction (XRD) and Raman spectroscopy measurements. **Figure 2**a shows the XRD patterns of the

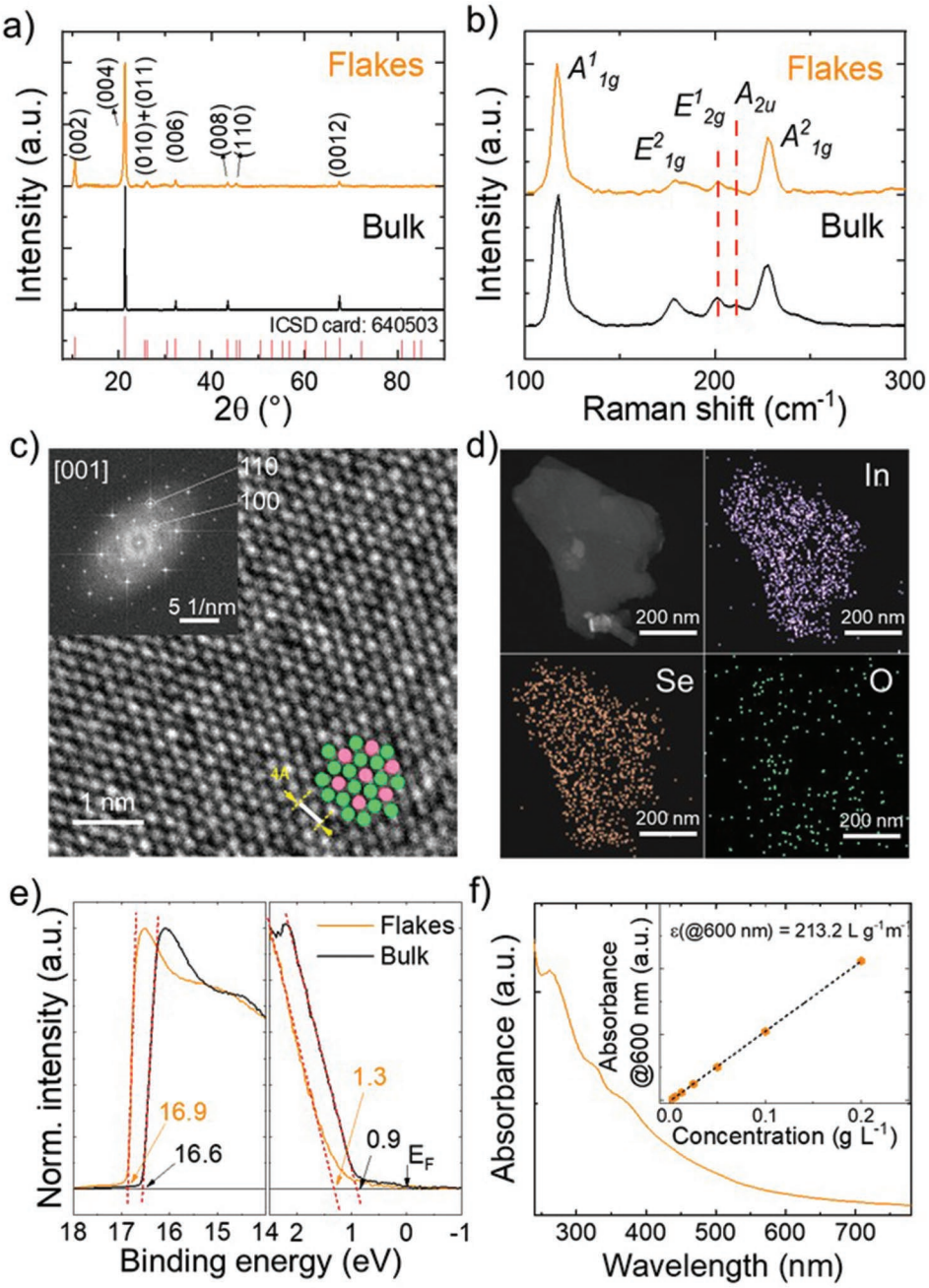

Figure 2. a) XRD patterns and b) Raman spectra (excitation wavelength = 633 nm) of InSe bulk (fragments of the as-growth InSe crystal) and flakes. The panels respectively report the diffraction peaks and the Raman modes attributed to the hexagonal β-InSe structure. The reference XRD pattern of β-InSe (ICSD card: 640 503) is also shown (red bars in panel a). c) HR-TEM image of a portion of InSe flake. The lattice spacing is also shown. The inset shows the corresponding FFT with reflections matching the ones of the hexagonal β-InSe structure (ICSD card: 640503). d) STEM-EDS analysis for a representative InSe flakes, showing the EDS maps for In ($L\alpha$ = 3.29 eV, violet), Se ($L\alpha$ = 1.37 eV, orange) and O ($K\alpha$ = 0.52, green). e) Normalized secondary electron cutoff region (left panel) and the region near the E_F (i.e., VB region) of the UPS spectra of InSe bulk and flakes, showing the onset energies. E_F corresponds to the zero of the binding energy scale. f) Absorption spectrum of the LPE-produced InSe flake dispersion, the top-right inset panel reports the absorbance (@600 nm) versus concentration plot, together with its linear fitting from whose slope the molar extinction coefficient has been extrapolated.

exfoliated samples, in comparison with that of the native bulk crystals. The positions of the diffraction peaks of both samples match those of the hexagonal β-InSe structure (D^4_{6h} symmetry, $P63/mmc$ space group, ICSD card: 640503),[58,70] whose crystallographic lattice parameters are a = b = 4.005 ± 0.004 Å and c = 16.660 ± 0.004 Å.[71] Compared to the bulk crystal, the InSe flakes exhibit additional XRD peaks because of their random orientation. The bulk sample preferentially shows the diffraction peaks belonging to the {00*l*} family, indicating a preferential placement of the crystal fragment perpendicular

to the *c* axis. Contrary, the exfoliated sample exhibits peaks associated with other planes (e.g., 010, 110, and 011), likely due to a disordered arrangement of the flakes. Figure 2b shows the Raman spectra of the bulk and exfoliated samples. According to the group theory, β-InSe has six active Raman modes, namely $2A_{1g}$, $2E_{1g}$, E^1_{2g}, A_{2u}.[72] Consistently with this theoretical consideration, bulk and exfoliated samples show these peaks at similar positions, i.e., A^1_{1g} at ≈117 cm^{-1}, E^2_{1g} at ≈179 cm^{-1}, E^1_{2g} at ≈201 cm^{-1}, A_{2u} at ≈210 cm^{-1}, A^2_{1g} at ≈227 cm^{-1}, in agreement with previous experimental studies.[70] The absence of extra peaks in the exfoliated sample suggests that the LPE process effectively preserves the chemical and crystalline integrity of the native crystals. High-resolution TEM (HR-TEM) measurements were performed to further elucidate the structural properties of the exfoliated sample. Figure 2c reports a HR-TEM image of a portion of the InSe flake, whose lattice spacings and the reflections in the fast Fourier transform (FFT; in inset) match those of the hexagonal β-InSe structure (ICSD card: 640503), in agreement with XRD data. Figure 2d shows the scanning TEM coupled with EDS (STEM-EDS) characterization of InSe flakes, whose elemental analysis (Table S2, Supporting Information) indicates a nearly ideal InSe stoichiometry (Se-to-In atomic ratio of ≈1.06), together with a low oxygen atomic content (O-to-In atomic ratio ≈0.3). Considering that the oxygen signal originated also outside the InSe flakes, our results indicate that InSe flakes preserve their chemical integrity upon exposure to ambient conditions.[70] Ultraviolet photoelectron spectroscopy (UPS) and UV/visible absorbance spectroscopy measurements were performed to gain information on the optoelectronic properties of InSe flakes, in comparison to those of the as-grown bulk crystal. Figure 2e shows the secondary electron cut-off region of He I (21.22 eV) UPS spectra measured for the InSe bulk and flakes. The cut-off energies are 16.6 eV for InSe bulk and 16.9 eV for InSe flakes, corresponding to work function (WF) values of 4.6 and 4.3 eV, respectively. These values are similar to those predicted by DFT calculation.[73] The region near the Fermi level (E_F) of the UPS spectra indicates that E_{VBM} values are −5.5 and −5.6 eV (vs vacuum level) for the InSe bulk and flakes, respectively. The differences in WF and E_{VBM} may arise from the presence of defective edges and the presence of quantum confinement effects in the exfoliated sample.[73] Figure 2f shows the absorbance spectrum of the LPE-produced InSe dispersion, showing three features at ≈265, 330, and ≈370 nm that are ascribed to the electronic direct transitions from deep valence bands (degenerate Se-$p_{x/y}$ orbitals dominated) to the conduction band (In-s orbital dominated) of InSe flakes.[32,35,70] The long absorbance tail observed in the green/red spectral region is instead associated with the bandgap transitions involving the valence band maximum (Se-p_z orbital dominated) and the conduction band minimum (In-s orbital dominated) in the vicinity of the Γ point, in agreement with previous studies.[32,68] Since these bandgap transitions are forbidden or extremely weak for in-plane polarized light allowed only for out-of-plane polarized light,[32] the corresponding absorbance peaks are weaker compared to those observed in the UV/blue spectral region. Noteworthy, the peaks of the absorbance spectrum are the results of the overlap between the optical features since our sample consists of flakes with polydisperse morphological characteristics (see Figure 1c–e). As mentioned before, previous DFT calculations have shown a strong relation between the thickness of the flakes and their optoelectronic characteristics due to the confinement effect.[32,35,70] The significant change in the optical bandgap of InSe with varying thickness has been explained by the interlayer coupling sensitivity of the out-of-plane oriented Se-p_z orbital that is involved in the bandgap transition with the smallest energy. The molar extinction coefficient -$\varepsilon(\lambda)$- of the InSe flakes was estimated using the Lambert-Beer law by measuring the absorbance spectra of controlled dilutions/concentrations of the LPE-produced InSe dispersion, whose initial concentration (0.2 ± 0.02 g L^{-1}) was first measured by gravimetric method, i.e., by drying the dispersion under N_2 flux and weighting the remaining solid powder. The linear fitting of the absorbance (@600 nm) versus concentration plot (inset of Figure 2f) provides an ε(600 nm) of the InSe flakes of 213.1 L g^{-1} m^{-1}. This parameter was used to control the concentration among different batches of InSe dispersion so that the amount of material deposited for the realization of films was properly controlled.

2.2. ITO NCs Synthesis and Characterization

ITO NCs were produced through a continuous growth process,[51,74] in which a degassed solution of the precursors consisting of tin(IV) acetate, indium(III) acetate, and oleic acid mixture (1:9 Sn-to-In atomic ratio, to reach a concentration of 0.5 mmol mL^{-1} oleic acid) was slowly injected (rate = 0.35 mL min^{-1}) in oleyl alcohol at 290 °C. To provide conductive ITO NCs, the insulating organic ligands of ITO NCs were stripped by slightly modifying the procedure reported in previous works,[75] as detailed in the Experimental Section (Supporting Information). Bright-field transmission electron microscopy measurements were performed to confirm the successful formation of ITO NCs and to determine their size. **Figure 3**a reports a BF-TEM image of ITO NCs, showing that they have a nearly rounded shape with an average diameter of 10.8 nm ± 1.9 nm, as shown from the distribution of their size (Figure 3b). Being a well-established approach to assessing the relative number of Sn dopants in ITO NCs,[76] inductively coupled plasma optical emission spectrometry (ICP-OES) was performed as a volume-sensitive technique to estimate the doping levels of the ITO NCs, estimating a Sn doping concentration of 11.5%. Noteworthy, degenerately doped metal oxide NCs are capable of withstanding extraordinarily high levels of doping without deteriorating their internal morphological structure.[77] In the case of ITO NCs, the doping mechanism involves aliovalent substitutional doping with donor impurities represented by the Sn atoms.[78] For this reason, the optoelectronic properties of ITO NCs are extremely sensitive to the concentration of tin dopants with higher values of Sn resulting in higher carrier densities, higher conductivity, and blue-shifted localized plasmonic surface resonance (LPSR). Accordingly, the doping concentration can be estimated from absorbance measurements, being the absorption spectrum of highly-doped metal oxide nanocrystals characterized by a strong LPSR.[79] The latter is generated by free electrons confined in the nanocrystal volume that resonate with the incoming radiation. Therefore, the presence of a plasmonic response can be an indication of the metallic

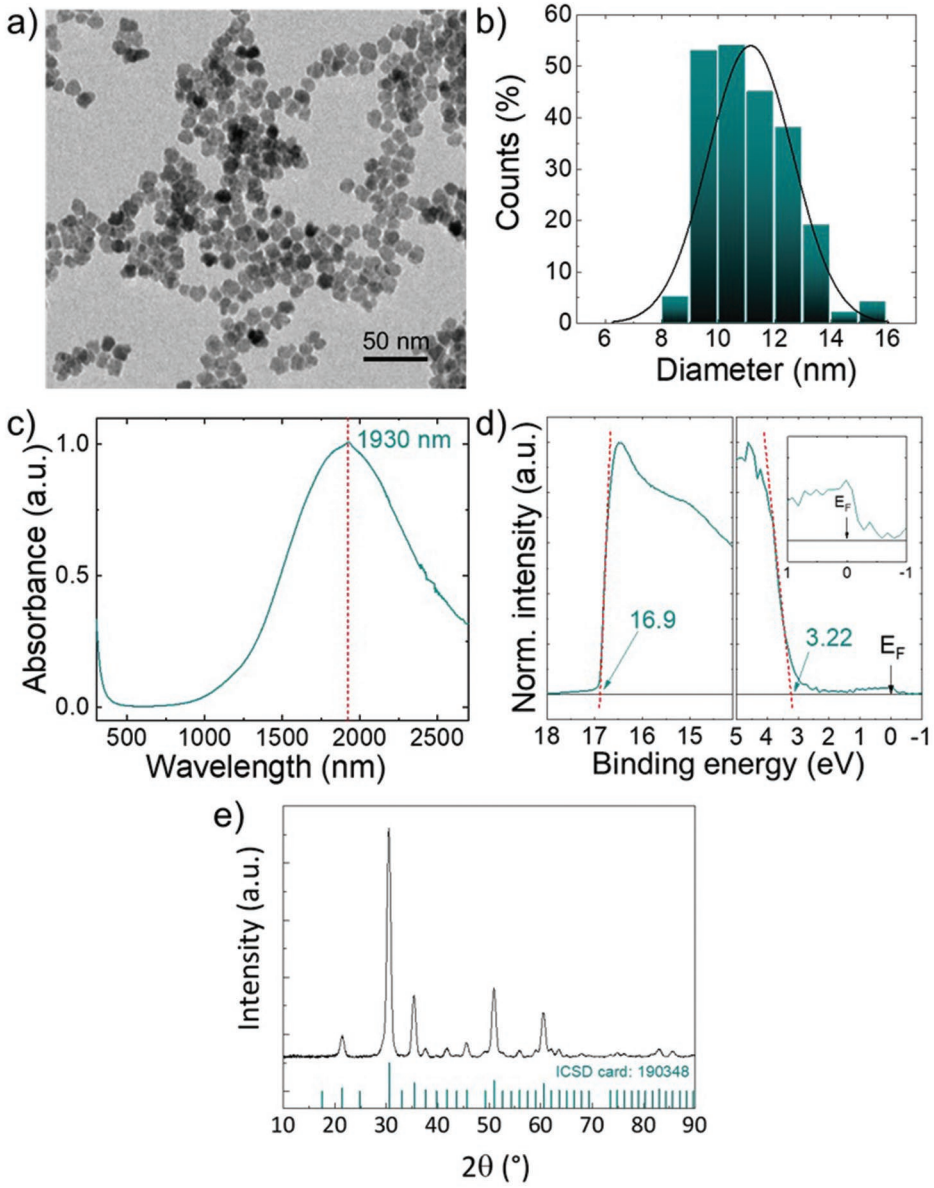

Figure 3. a) BF-TEM image of ITO NCs without organic ligands. b) Statistical analysis of the diameter of ITO NCs, as calculated from the analysis of the BF-TEM images. c) Absorbance spectrum of ITO NCs dispersed in n-hexane, showing the LPSR peak position at 1930 nm and the optical absorption of inter-band transition in the UV range. d) Normalized secondary electron cut-off region (left panel) and the region near the E_F (i.e., VB region) of the UPS spectra of ITO NCs, showing the onset energies. e) XRD pattern of ITO NCs. The reference XRD pattern of In_2O_3 with a cubic bixbyite structure (ICSD card: 190348) is also shown (cyan bars).

behavior of these systems. The plasmonic properties of doped ITO NCs can be described according to the Mie scattering theory in the quasi-static approximation.[80] Metal oxide NCs optical response is characterized by the polarizability of the free electrons, described in the Drude-Lorentz model with the complex dielectric permittivity $\varepsilon(\omega) = \varepsilon_\infty - \omega_p^2/(\omega^2 + i\omega\Gamma)$, in which ω_p is the bulk plasma frequency, Γ is a damping parameter accounting for electron–electron scattering and ε_∞ is the high-frequency dielectric constant. More in detail, the LSPR is highly sensitive to the free carrier density, and hence the doping levels of the metal oxide NC, the size, and the dielectric surrounding of the nanocrystals.[51,81] The LSPR frequency (ω_{LSPR}) is found to be proportional to $\omega_p = (n_e e^2/\varepsilon_0 m^*)^{0.5}$, in which n_e is the free carrier density, ε_0 is the vacuum permittivity, e is the elementary charge and m^* is the effective electron mass.[81] Hence, it is possible to link the absorption properties to the electronic structure of the system. As shown in Figure 3c, the synthesized ITO NCs show a clear LSPR in the near-infrared (NIR) spectral region, with a ω_{LSPR} of ≈1.9 µm, as expected from literature data reported for similar sizes and doping levels.[51] We estimated $n_e \approx 1 \times 10^{27}$ m^{-3} by applying a fitting model based on Mie scattering theory and the Drude-Lorentz dielectric function to the absorption spectrum

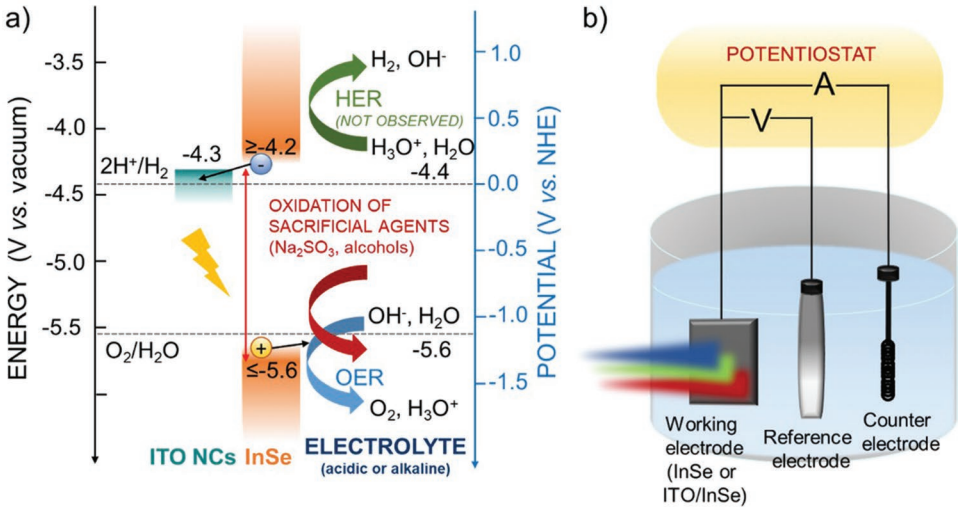

Figure 4. a) Energy level diagram of the PEC-type hybrid ITO/InSe photodetectors, whose working mechanism is also illustrated. The energy level of the materials (E_{CBM} and E_{VBM} of InSe and E_F of the ITO NCs have been extrapolated from our spectroscopic characterization (UPS and absorption data). b) Sketch of the electrochemical setup (three-electrode configuration system) used for the PEC characterization of the photodetectors, showing the working electrode, namely InSe or ITO/InSe photoelectrodes, reference electrode (KCl-saturated Ag/AgCl and 4.24 M KOH-filled Hg/HgO) and counter electrode (glassy carbon rod).

(more details in Supporting Information).[75,76] This data confirms the metallic behavior of the ITO NCs, which can therefore be used to electrically connect the InSe flakes in hybrid ITO/InSe photoactive films. In addition, the transport of charge carriers across heterointerfaces is regulated by the material energy-level alignment.[82] Therefore, UPS measurements were carried out to determine the WF of the ITO NCs from the energy onset in the high-energy region of their UPS spectrum (i.e., secondary electron cut-off). Figure 3d reports the He I (21.22 eV) UPS spectrum of the ITO NCs, whose cutoff energy (≈16.9 eV) corresponds to a WF of 4.3 eV. The region near the E_F of the UPS spectrum reveals that E_{VBM} is –7.5 eV (vs vacuum level). The structural properties of the ITO NCs were evaluated through XRD measurements. As shown in Figure 3e, the XRD pattern of our ITO NCs match that of In_2O_3 with a cubic bixbyite structure (ICSD card: 190348), in agreement with previous literature.[83] The broadening of the peaks is characteristic of colloidal nanoparticles.

2.3. Characterization of PEC-Type InSe and Hybrid ITO/InSe Photodetectors

Based on the above spectroscopic and optical characterizations of InSe flakes and ITO NCs, **Figure 4**a reports a sketch of the expected energy level diagram of the hybrid PEC-type ITO/InSe photodetectors operating in aqueous media. The working mechanism of these photodetectors proceeds through the following steps: 1) InSe flakes absorb visible light, exciting electrons from the VB to the CB; 2) the photogenerated electrons are collected by ITO NCs, while the holes are transferred to the electrolyte, driving an oxidation reaction, such as oxygen evolution reaction (OER) or oxidation of other chemicals (namely sacrificial agents, e.g., Na_2SO_3 and alcohols), at the InSe/electrolyte interface (in absence of ITO NCs, the electrons are transported by InSe flakes to the current collectors); 3) the electrons are transported to the current collector through the conductive network formed by ITO NCs, and then transferred to a counter electrode (such as Pt). The latter closes the circuit by reducing the electrolyte species. The third step can be visualized by the experimental setup (three-electrode configuration system) used for the PEC characterization of our InSe and hybrid ITO/InSe films (Figure 4b), as detailed in the Experimental Method section, Supporting Information. Noteworthy, the 2D morphology of InSe flakes intrinsically guarantees that the holes and electrons are photogenerated at the InSe/electrolyte and ITO/InSe interface, respectively, thus limiting charge recombination pathways, which can instead occur in bulk photoactive material.[9,10] In principle, and according to previous theoretical calculations,[84,17] the photogenerated electrons should have sufficient energy to drive the hydrogen evolution reaction (HER). However, as described hereafter, a poor cathodic photoresponse was observed for both InSe and hybrid ITO/InSe photoelectrodes. We speculate that the n-type doping of both InSe flakes and ITO NCs, as inferred from UPS and absorption spectroscopy analyses, may cause an upward band bending/dipole at the interface with the electrolyte, resulting in an energy barrier for the electrons to overcome in order to carry out the electrolyte reduction processes.[16] To produce our solution-processed PEC-type photodetectors, the dispersion on InSe flakes or mixture of InSe flakes and ITO NCs were deposited by spray coating onto a pyrolytic graphite substrate, the latter acting as current collector, following protocols described in previous works.[15,16] The photoresponses of the as-produced photoelectrodes were first evaluated for three different illumination wavelengths in the visible spectral range, namely 455, 505, and 625 nm. The photon energies corresponding to these illumination wavelengths are above the E_g of few-layer InSe flakes.

Figure 5a reports the responsivity versus potential plots for InSe photoelectrodes (without ITO NCs and a mass loading of InSe flakes of 0.2 mg cm^{-2}) at the investigated illumination wavelength,

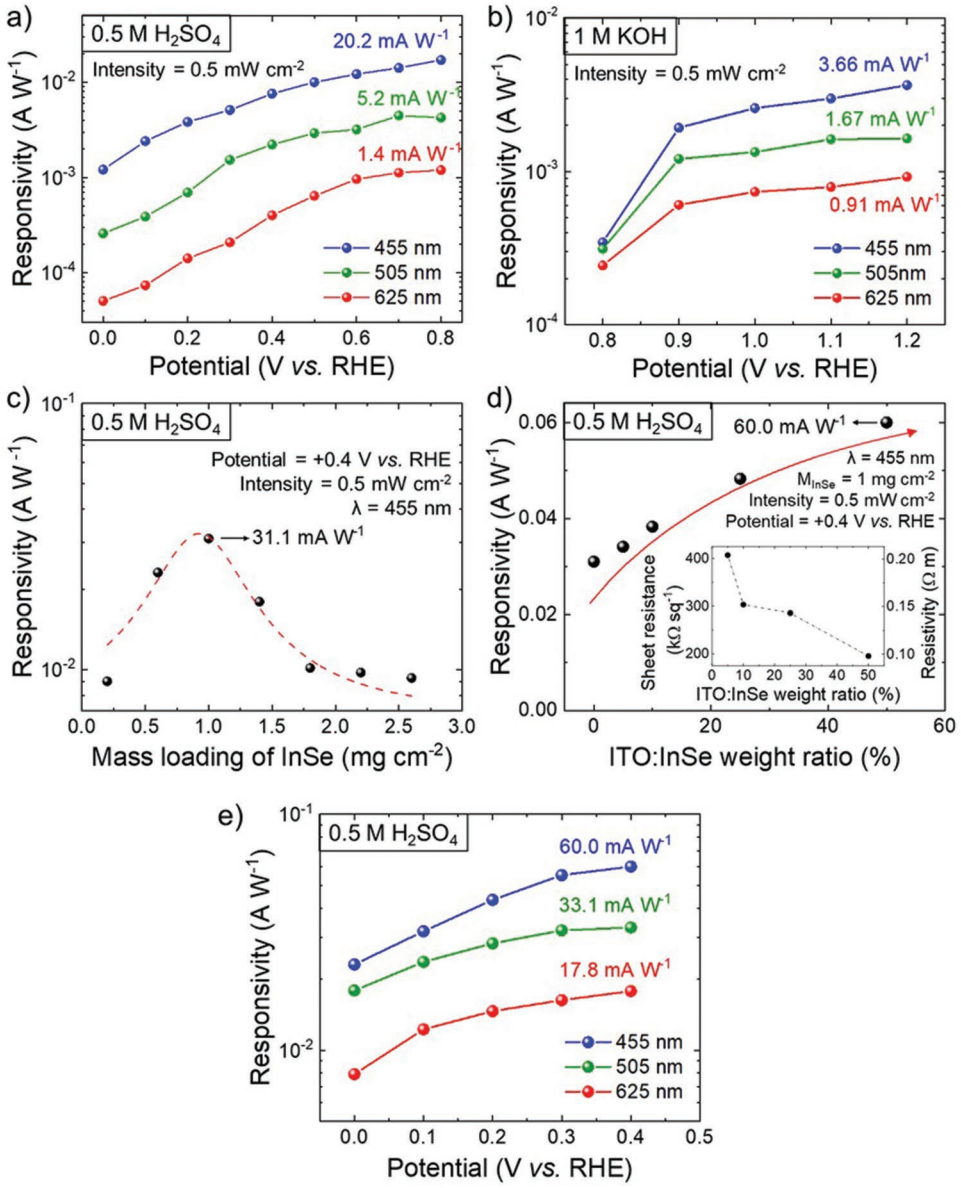

Figure 5. a) Responsivity of the solution-processed PEC-type InSe photodetectors as a function of the applied potential in 0.5 M H_2SO_4 under three different illumination wavelengths in the visible spectral range: 455, 505, and 625 nm (intensity: 0.5 mW cm^{-2}). b) Responsivity of the InSe photodetectors as a function of the applied potential in 1 M KOH, under 0.5 mW cm^{-2} 455, 505 and 625 nm illuminations. c) Responsivity of the InSe photodetectors as a function of M_{InSe} in 0.5 M H_2SO_4 at +0.4 V versus RHE under 0.5 mW cm^{-2} 455 nm illumination. d) Responsivity of the InSe photodetectors as a function of the ITO:InSe weight ratio (%) in in 0.5 M H_2SO_4 at +0.4 V versus RHE under 0.5 mW cm^{-2} 455 nm illumination (M_{InSe} = 1 mg cm^{-2}). The inset panel reports the R_{sh} and ρ of ITO/InSe films as a function of the ITO:InSe weight ratio (%). e) Responsivity of hybrid ITO/InSe photodetectors as a function of the applied potential in 0.5 M H_2SO_4 under three different illumination wavelengths in the visible spectral range: 455, 505, and 625 nm (intensity: 0.5 mW cm^{-2}).

as calculated from linear sweep voltammetry (LSV) measurements at the illumination intensity of 0.5 mW cm^{-2} in 0.5 M H_2SO_4. The applied potentials were constrained within values corresponding to dark current density inferior to 50 μA cm^{-2}, leading to an on-off signal ratio between 0.01 and 10, depending on the applied potential. It is worth noticing that PEC-type photodetectors commonly show a low on–off ratio compared to other solid-state technologies. Nevertheless, the possibility to couple them with compact lock-in system can substantially reduce the background (off) signal to the noise of the lock-in detection system.[7,85] Consequently, thanks to their differential mode operation, PEC-type photodetectors can show high resolution and sensitivity in several applications. For example, PEC sensors can outperform conventional electrochemical sensors in terms of sensitivity, while avoiding the need for frequent recalibration.[7,8] The responsivity of the photodetectors increases with decreasing the wavelength, indicating that the photons with the highest energy (e.g., ≈2.7 eV for illumination wavelength = 455 nm)

can efficiently generate charge carriers from both Se-$p_{x/y}$-to-In-s and Se-p_z-to-In-s direct transitions.[32,35,70] No photocathodic response was observed for InSe photoelectrodes at applied potential higher than 0 V versus RHE. These results agree with previous studies,[41] in which films of InSe flakes exhibited a photoanodic response in alkaline media. In addition, the photoanodic response of our photoelectrodes in 0.5 M H_2SO_4 (responsivity = 20.2 mA W^{-1} at +0.8 V vs RHE for 455 nm illumination) was one order of magnitude higher than the one observed in 1 M KOH (e.g., 3.7 mA W^{-1} at +1.2 V vs RHE for 455 nm illumination) (Figure 5b), proving for the first time the potential of InSe flakes for PEC applications in acidic media. Figure 5c shows the responsivity of the photoelectrodes as a function of the InSe mass loading (M_{InSe}) in 0.5 M H_2SO_4. By fixing the applied potential at +0.4 V versus RHE, a maximum responsivity of 31. mA W^{-1} was reached at M_{InSe} = 1 mg cm^{-2}. This means that this photoactive material mass loading guarantees an optimal absorption (i.e., poor light transmission loss) of the incident light by InSe flakes. By further increasing M_{InSe}, the photoelectrode responsivity decreases because of the excessive thickness of the photoactive films, which are not capable of efficiently transporting electrons photogenerated near film surface towards the current collectors. To solve the dichotomy between absorption and charge transport performance, electrically conductive ITO NCs were therefore hybridized with InSe flakes to create an electron transport pathway, as previously discussed and schematized in Figure 4a. Figure 5d shows the responsivity of the hybrid ITO/InSe photoelectrodes as a function of the weight content of ITO NCs compared to one of the InSe flakes (M_{InSe} fixed at 1 mg cm^{-2}). For ITO-to-InSe weight ratio of 50%, the hybrid photoelectrodes reached a maximum responsivity of 60.0 mA W^{-1} at +0.4 V versus RHE, which corresponds to a EQE of 16.4% and represents a +60.8% responsivity increase compared to the photoelectrodes without ITO NCs. The sheet resistance (R_{sh}) of InSe/ITO hybrid films as a function of the ITO:InSe weight ratio was measured by four-probe method. According to the results obtained, the InSe film without the presence of ITO nanocrystals did not show a measurable R_{sh} due to the semiconductive nature of the network composed of randomly dispersed InSe flakes. The effects of ITO nanocrystals content on electrical conductivity are shown in the inset of Figure 5d. The R_{sh} and the resistivity ($\rho = R_{sh} \times t_{film}$, where t_{film} is the average thickness of the films measured by profilometry on the samples of ITO/InSe films) decrease with increasing the content of ITO NCs from 5 to 50 wt%. Noteworthy, the photoelectrodes based on only ITO NCs exhibited a nondetectable photocurrent density for all the investigated illumination wavelength, thus excluding the participation of ITO NCs in charge photogeneration processes. In addition, the hybrid ITO/InSe photoelectrodes did not exhibit any photoresponse in 1 M KOH, probably because of the instability/dissolution of ITO NCs in alkaline media. In particular, the Pourbaix diagram of In suggests the possible formation of InO_2^- species in strong alkaline media (pH > 11) and anodic potentials.[86] Figure 5e reports the responsivity of hybrid ITO/InSe photodetectors as a function of the applied potential in 0.5 M H_2SO_4 under the investigated illumination wavelengths (intensity: 0.5 mW cm^{-2}), showing a similar trend to that of the InSe photodetector (i.e., the responsivity increases with decreasing the wavelength, which is consistent with the absorbance spectrum of InSe flakes). Table S3 (Supporting Information) lists the performances of the representative PEC-type photodetectors and other solution-processed photodetectors reported in literature, showing that our ITO/InSe photoelectrodes feature excellent responsivities for 0.1–1 mW cm^{-2} illumination intensity range.

To assess the stability of our InSe and hybrid ITO/InSe photoelectrodes, their responsivity was evaluated over subsequent LSV scans. Regrettably, the InSe photoelectrodes have shown poor stability over subsequent LSV scans in both 0.5 M H_2SO_4 and 1 M KOH (**Figure 6**a). To solve this important issue, two sacrificial agents, e.g., IPA and Na_2SO_3 were added to the electrolyte, since they (or their anions, i.e., SO_3^{2-} for Na_2SO_3) represent electron donors (i.e., hole scavengers) that are easily oxidized, inhibiting or limiting, in principle, the PEC degradation (e.g., corrosion) of the photoelectrodes under anodic operation.[56,57,87] Indeed, as shown in Figure 4a, E_{VBM} of InSe is enough negative to promote the oxidation of organic (e.g., alcohols) and inorganic (e.g., Na_2SO_3) compounds. In particular, IPA can be decomposed to produce organic compounds (e.g., acetone) and H_2,[56,57,87] while the SO_3^{2-} can be oxidized to SO_4^{2-}, limiting concomitant photocatalyst oxidation/corrosion.

In 0.5 M H_2SO_4, the sacrificial agents improve the stability of the photoelectrodes, even though still degraded significantly (Figure 6b). In particular, the photoelectrodes retained 50% of their initial responsivity after 20 LSV scans at 0.35 V versus RHE in presence of 20% vol of IPA. For hybrid ITO/InSe electrodes, the use of 0.35 M Na_2SO_3 as sacrificial agent leads to the best stability (–63.8% responsivity after 20 LSV scans, Figure 6c), indicating the need to implement a more effective strategy to stabilize the photoelectrodes. In addition, even though the sacrificial agents increased the stability of the photoelectrodes, their responsivity decreased from 31.1 mA W^{-1} (without sacrificial agents) to 5.2 and 1.98 mA W^{-1} in presence of 20% vol. IPA and 0.35 M Na_2SO_3 sacrificial agents, respectively. These data indicate that the exploitation of PEC properties of InSe flakes in acidic media, in which they show the highest responsivity, is presently still challenging because of their poor stability. Meanwhile, in 1 M KOH with 0.35 M Na_2SO_3, the InSe photodetectors improved the performance over time (+43.5% responsivity after 20 LSV scans, Figure 6d) without significantly affecting the responsivity (1.3 mA W^{-1} at +1 V vs RHE). Our preliminary data suggest that the effectiveness of a sacrificial agent is pH-dependent, and this behavior may be generally explained by considering that the oxidation of a photoactive material also depends on the pH. Prospectively, beyond the identification of a suitable operating pH range, the screening of other sacrificial agents beyond those here investigated may further lead to an improvement of the overall stability of InSe and ITO/InSe photodetectors. Despite their preliminary nature, our results indicate that established stabilizing strategies based on the use of sacrificial agents can be effectively explored also for the case of metal monochalcogenide-based photo(electro)catalysts. Meanwhile, our results also remark the potential of InSe flakes for PEC applications in alkaline media, in agreement with previous studies,[41] which however reported three orders of magnitude lower values of responsivity (on the order of few μA W^{-1}) under alkaline media.

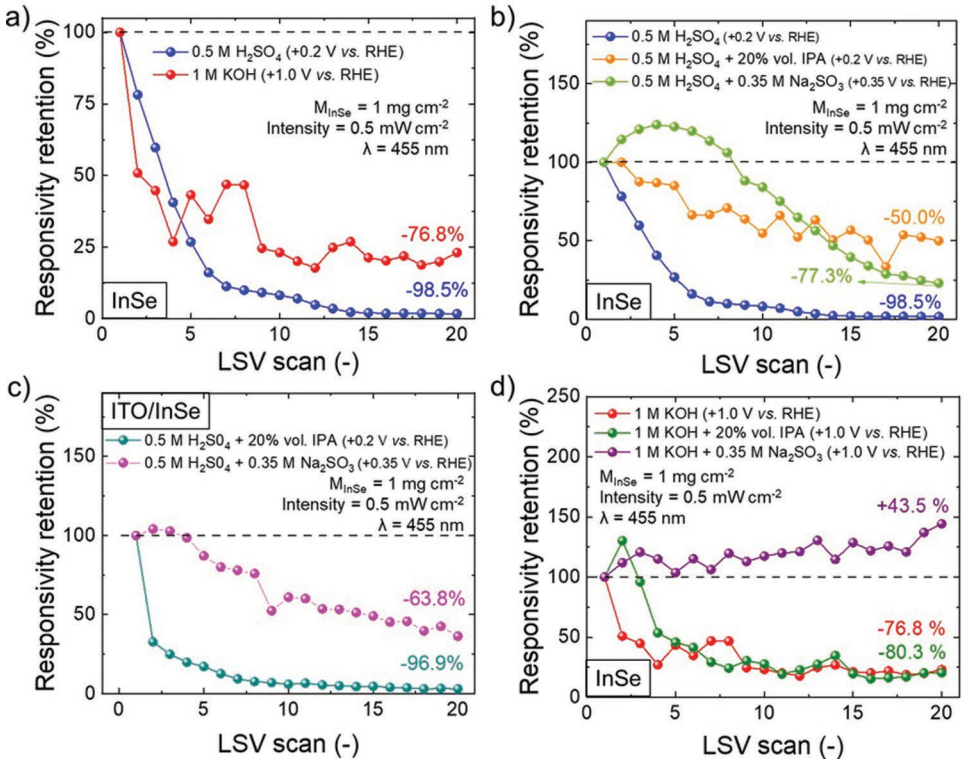

Figure 6. a) Responsivity retention of the InSe photodetectors in: 0.5 M H_2SO_4 at +0.2 V versus RHE and 1 M KOH at +1.0 V versus RHE under 0.5 mW cm^{-2} 455 nm illumination (M_{InSe} = 1 mg cm^{-2}). b) Responsivity retention of the InSe photodetectors in: 0.5 M H_2SO_4 at +0.2 V versus RHE, 0.5 M H_2SO_4 + 20% vol IPA at +0.2 V versus RHE, and 0.5 M H_2SO_4 + 0.35 M Na_2SO_4 at +0.35 V versus RHE, under 0.5 mW cm^{-2} 455 nm illumination (M_{InSe} = 1 mg cm^{-2}). c) Responsivity retention of the hybrid ITO/InSe photodetectors in: 0.5 M H_2SO_4 + 20% vol. IPA at +0.2 V versus RHE, and 0.5 M H_2SO_4 + 0.35 M Na_2SO_4 at +0.35 V versus RHE, under 0.5 mW cm^{-2} 455 nm illumination (M_{InSe} = 1 mg cm^{-2}). d) Responsivity retention of the InSe photodetectors in: 1 M KOH at +1.0 V versus RHE, 1 M KOH + 20% vol. IPA at +1.0 V versus RHE, and 1 M KOH + 0.35 M Na_2SO_4 at +1.0 V versus RHE, under 0.5 mW cm^{-2} 455 nm illumination (M_{InSe} = 1 mg cm^{-2}).

3. Conclusions

We reported the PEC characterization of LPE-produced InSe flakes for their application as solution-processed photoactive films in PEC-type photodetectors in aqueous media, including acidic and alkaline solutions. To provide new insights into the use of 2D InSe in practical devices, ITO NCs were evaluated to electrically connect InSe flakes, providing efficient charge transport pathways in hybrid photoactive ITO/InSe films. Remarkable photoanodic responses of InSe and hybrid ITO/InSe photoelectrodes were observed both in 0.5 M H_2SO_4 and 1 M KOH. The highest photoresponse of the InSe photoelectrodes was observed in acidic media (0.5 M H_2SO_4), reaching responsivities up to 31.1 mA W^{-1} at 0.8 V versus RHE under 0.5 mW cm^{-2} 455 nm illumination. By hybridizing the InSe flakes with ITO NCs and optimizing the thickness of the hybrid film films, hybrid ITO/InSe photodetectors achieved a responsivity up to 60.0 mA W^{-1} (EQE = 16.3%) at +0.4 V versus RHE under the same illumination condition. Our experimental data show that both InSe and ITO/InSe-based photoelectrodes have a progressive degradation of their responsivity over subsequent LSV scans, indicating the need to implement adequate strategies for practical development. We attempted to improve the stability of the photoelectrodes by adding prototypical sacrificial agents, e.g., IPA and Na_2SO_3, in the electrolytes. While in 0.5 M H_2SO_4 the stability of the photoelectrodes was still insufficient, the InSe photoelectrodes have shown +43.5% of responsivity over subsequent LSV scans in 1 M KOH and 0.35 M Na_2SO_3. Our results shed light on the potential of 2D InSe for aqueous PEC-type applications while outlining the existing challenges related to their stability under anodic operation.

Supporting Information

Supporting Information is available from the Wiley Online Library or from the author.

Acknowledgements

G.B. and M.I.Z. contributed equally to this work. This project has received funding from the European Union's Horizon 2020 European Research Council under grant agreement no. [850875] (Light-DYNAMO) and from the European Union's Horizon 2020 Research and Innovation programme under grant agreement no. [101017821] (LIGHTCAP) and grant agreement no. 881603-GrapheneCore3, the MSCA-ITN ULTIMATE project under grant agreement no. 813036, and the Bilateral project GINSENG between NSFC (China) and MAECI (Italy) (2018–2020) by the Natural Science Foundation of Shandong Province (ZR2019QEM009). Z.S. was supported by Czech Science Foundation (GACR No. 20-16124J). A.S. was supported by the European Union's Horizon 2020 research

and innovation programme under grant agreement No 956813. The authors thank the Materials Characterization Facility—Istituto Italiano di Tecnologia—for the support in XRD data acquisition/analysis and Electron Microscopy facility—Istituto Italiano di Tecnologia—for the support in TEM data acquisition.

Open Access Funding provided by Istituto Italiano di Tecnologia within the CRUI-CARE Agreement.

Conflict of Interest

The authors declare no conflict of interest.

Data Availability Statement

The data that support the findings of this study are available from the corresponding author upon reasonable request.

Keywords

2D materials, energy conversion, photodetectors, photoelectrochemical cells, solution processing

Received: August 9, 2022
Revised: September 16, 2022
Published online: October 20, 2022

[1] S. K. Saraswat, D. D. Rodene, R. B. Gupta, *Renewable Sustainable Energy Rev.* **2018**, *89*, 228.
[2] E. Mousset, D. D. Dionysiou, *Environ. Chem. Lett.* **2020**, *18*, 1301.
[3] J. Shu, D. Tang, *Anal. Chem.* **2020**, *92*, 363.
[4] J. Zhou, L. Chen, Y. Wang, Y. He, X. Pan, E. Xie, *Nanoscale* **2016**, *8*, 50.
[5] Y. Luo, D. Wang, Y. Kang, X. Liu, S. Fang, M. H. Memon, H. Yu, H. Zhang, D. Luo, X. Sun, B. S. Ooi, C. Gong, Z. Xu, H. Sun, *Adv. Opt. Mater.* **2022**, *10*, 2102839.
[6] C. Zhao, Y. He, X. Wang, W. Sun, *Sens. Actuators, B* **2021**, *328*, 128992.
[7] S. Bellani, A. Ghadirzadeh, L. Meda, A. Savoini, A. Tacca, G. Marra, R. Meira, J. Morgado, F. Di Fonzo, M. R. Antognazza, *Adv. Funct. Mater.* **2015**, *25*, 4531.
[8] R. María Girón, J. Marco-Martínez, S. Bellani, A. Insuasty, H. Comas Rojas, G. Tullii, M. R. Antognazza, S. Filippone, N. Martín, *J. Mater. Chem. A* **2016**, *4*, 14284.
[9] Y. Li, Y.-L. Li, B. Sa, R. Ahuja, *Catal. Sci. Technol.* **2017**, *7*, 545.
[10] T. Su, Q. Shao, Z. Qin, Z. Guo, Z. Wu, *ACS Catal.* **2018**, *8*, 2253.
[11] G. Bianca, C. Trovatello, A. Zilli, M. I. Zappia, S. Bellani, N. Curreli, I. Conticello, J. Buha, M. Piccinni, M. Ghini, M. Celebrano, M. Finazzi, I. Kriegel, N. Antonatos, Z. Sofer, F. Bonaccorso, *ACS Appl. Mater. Interfaces* **2022**, *14*, 34963.
[12] T.-F. Yeh, C.-Y. Teng, S.-J. Chen, H. Teng, *Adv. Mater.* **2014**, *26*, 3297.
[13] B. Mahler, V. Hoepfner, K. Liao, G. A. Ozin, *J. Am. Chem. Soc.* **2014**, *136*, 14121.
[14] Q. Zhang, W. Wang, J. Zhang, X. Zhu, Q. Zhang, Y. Zhang, Z. Ren, S. Song, J. Wang, Z. Ying, R. Wang, X. Qiu, T. Peng, L. Fu, *Adv. Mater.* **2018**, *30*, 1707123.
[15] M. I. Zappia, G. Bianca, S. Bellani, M. Serri, L. Najafi, R. Oropesa-Nuñez, B. Martín-García, D. Bouša, D. Sedmidubský, V. Pellegrini, Z. Sofer, A. Cupolillo, F. Bonaccorso, *Adv. Funct. Mater.* **2020**, *30*, 1909572.
[16] G. Bianca, M. I. Zappia, S. Bellani, Z. Sofer, M. Serri, L. Najafi, R. Oropesa-Nuñez, B. Martín-García, T. Hartman, L. Leoncino, D. Sedmidubský, V. Pellegrini, G. Chiarello, F. Bonaccorso, *ACS Appl. Mater. Interfaces* **2020**, *12*, 48598.
[17] Q. Peng, R. Xiong, B. Sa, J. Zhou, C. Wen, B. Wu, M. Anpo, Z. Sun, *Catal. Sci. Technol.* **2017**, *7*, 2744.
[18] M. I. Zappia, G. Bianca, S. Bellani, N. Curreli, Z. Sofer, M. Serri, L. Najafi, M. Piccinni, R. Oropesa-Nuñez, P. Marvan, V. Pellegrini, I. Kriegel, M. Prato, A. Cupolillo, F. Bonaccorso, *J. Phys. Chem. C* **2021**, *125*, 11857.
[19] F. M. Oliveira, J. Paštika, L. S. Pires, Z. Sofer, R. Gusmão, *Adv. Mater. Interfaces* **2021**, *8*, 2100294.
[20] B. Lin, A. Chaturvedi, J. Di, L. You, C. Lai, R. Duan, J. Zhou, B. Xu, Z. Chen, P. Song, J. Peng, B. Ma, H. Liu, P. Meng, G. Yang, H. Zhang, Z. Liu, F. Liu, *Nano Energy* **2020**, *76*, 104972.
[21] M. Zhu, Z. Sun, M. Fujitsuka, T. Majima, *Angew. Chem., Int. Ed.* **2018**, *57*, 2160.
[22] A. Naseri, M. Samadi, A. Pourjavadi, A. Z. Moshfegh, S. Ramakrishna, *J. Mater. Chem. A* **2017**, *5*, 23406.
[23] S. Ida, T. Ishihara, *J. Phys. Chem. Lett.* **2014**, *5*, 2533.
[24] D. Liu, J. Wang, S. Bian, Q. Liu, Y. Gao, X. Wang, P. K. Chu, X.-F. Yu, *Adv. Funct. Mater.* **2020**, *30*, 2002731.
[25] J. Low, J. Yu, W. Ho, *J. Phys. Chem. Lett.* **2015**, *6*, 4244.
[26] F. Bonaccorso, Z. Sun, T. Hasan, A. C. Ferrari, *Nat. Photonics* **2010**, *4*, 611.
[27] J. Wang, J. Han, X. Chen, X. Wang, *InfoMat* **2019**, *1*, 33.
[28] N. Curreli, M. Serri, D. Spirito, E. Lago, E. Petroni, B. Martín-García, A. Politano, B. Gürbulak, S. Duman, R. Krahne, V. Pellegrini, F. Bonaccorso, *Adv. Funct. Mater.* **2020**, *30*, 1908427.
[29] J. Kang, S. A. Wells, V. K. Sangwan, D. Lam, X. Liu, J. Luxa, Z. Sofer, M. C. Hersam, *Adv. Mater.* **2018**, *30*, 1802990.
[30] D. Boukhvalov, B. Gürbulak, S. Duman, L. Wang, A. Politano, L. Caputi, G. Chiarello, A. Cupolillo, *Nanomaterials* **2017**, *7*, 372.
[31] W. Feng, W. Zheng, W. Cao, P. Hu, *Adv. Mater.* **2014**, *26*, 6587.
[32] D. A. Bandurin, A. V. Tyurnina, G. L. Yu, A. Mishchenko, V. Zólyomi, S. V. Morozov, R. K. Kumar, R. V. Gorbachev, Z. R. Kudrynskyi, S. Pezzini, Z. D. Kovalyuk, U. Zeitler, K. S. Novoselov, A. Patanè, L. Eaves, I. V. Grigorieva, V. I. Fal'ko, A. K. Geim, Y. Cao, *Nat. Nanotechnol.* **2017**, *12*, 223.
[33] Y. Choi, H. Kim, J. Yang, S. W. Shin, S. H. Um, S. Lee, M. S. Kang, J. H. Cho, *Chem. Mater.* **2018**, *30*, 4527.
[34] J. Kim, S. S. Baik, S. H. Ryu, Y. Sohn, S. Park, B.-G. Park, J. Denlinger, Y. Yi, H. J. Choi, K. S. Kim, *Science* **2015**, *349*, 723.
[35] C. Song, S. Huang, C. Wang, J. Luo, H. Yan, *J. Appl. Phys.* **2020**, *128*, 060901.
[36] C. Backes, A. M. Abdelkader, C. Alonso, A. Andrieux-Ledier, R. Arenal, J. Azpeitia, N. Balakrishnan, L. Banszerus, J. Barjon, R. Bartali, S. Bellani, C. Berger, R. Berger, M. M. B. Ortega, C. Bernard, P. H. Beton, A. Beyer, A. Bianco, P. Bøggild, F. Bonaccorso, G. B. Barin, C. Botas, R. A. Bueno, D. Carriazo, A. Castellanos-Gomez, M. Christian, A. Ciesielski, T. Ciuk, M. T. Cole, J. Coleman, et al., *2D Mater.* **2020**, *7*, 022001.
[37] F. Bonaccorso, A. Bartolotta, J. N. Coleman, C. Backes, *Adv. Mater.* **2016**, *28*, 6136.
[38] J. H. Kim, D. Hansora, P. Sharma, J.-W. Jang, J. S. Lee, *Chem. Soc. Rev.* **2019**, *48*, 1908.
[39] E. Samuel, B. Joshi, M.-W. Kim, M. T. Swihart, S. S. Yoon, *Nano Energy* **2020**, *72*, 104648.
[40] A. Visan, J. R. van Ommen, M. T. Kreutzer, R. G. H. Lammertink, *Ind. Eng. Chem. Res.* **2019**, *58*, 5349.
[41] Z. Li, H. Qiao, Z. Guo, X. Ren, Z. Huang, X. Qi, S. C. Dhanabalan, J. S. Ponraj, D. Zhang, J. Li, J. Zhao, J. Zhong, H. Zhang, *Adv. Funct. Mater.* **2018**, *28*, 1705237.
[42] Y. Yan, R. W. Crisp, J. Gu, B. D. Chernomordik, G. F. Pach, A. R. Marshall, J. A. Turner, M. C. Beard, *Nat. Energy* **2017**, *2*, 17052.

[43] O. E. Semonin, J. M. Luther, S. Choi, H. Y. Chen, J. Gao, A. J. Nozik, M. C. Beard, *Science* **2011**, *334*, 1530.
[44] N. Curreli, M. Serri, M. I. Zappia, D. Spirito, G. Bianca, J. Buha, L. Najafi, Z. Sofer, R. Krahne, V. Pellegrini, F. Bonaccorso, *Adv. Electron. Mater.* **2021**, *7*, 2001080.
[45] X. Sheng, T. Xu, X. Feng, *Adv. Mater.* **2019**, *31*, 1805132.
[46] S. Bellani, L. Najafi, G. Tullii, A. Ansaldo, R. Oropesa-Nuñez, M. Prato, M. Colombo, M. R. Antognazza, F. Bonaccorso, *J. Mater. Chem. A* **2017**, *5*, 25177.
[47] A. Agrawal, R. W. Johns, D. J. Milliron, *Annu. Rev. Mater. Res.* **2017**, *47*, 1.
[48] J. N. Anker, W. P. Hall, O. Lyandres, N. C. Shah, J. Zhao, R. P. Van Duyne, *Nat. Mater.* **2008**, *7*, 442.
[49] M. Ghini, A. Rubino, A. Camellini, I. Kriegel, *Nanoscale Adv.* **2021**, *3*, 6628.
[50] Y. Wang, E. L. Runnerstrom, D. J. Milliron, *Annu. Rev. Chem. Biomol. Eng.* **2016**, *7*, 283.
[51] B. M. Crockett, A. W. Jansons, K. M. Koskela, D. W. Johnson, J. E. Hutchison, *ACS Nano* **2017**, *11*, 7719.
[52] C. M. Staller, Z. L. Robinson, A. Agrawal, S. L. Gibbs, B. L. Greenberg, S. D. Lounis, U. R. Kortshagen, D. J. Milliron, *Nano Lett.* **2018**, *18*, 2870.
[53] I. Kriegel, M. Ghini, S. Bellani, K. Zhang, A. W. Jansons, B. M. Crockett, K. M. Koskela, E. S. Barnard, E. Penzo, J. E. Hutchison, J. A. Robinson, L. Manna, N. J. Borys, P. J. Schuck, *J. Phys. Chem. C* **2020**, *124*, 8000.
[54] M. Ghini, E. S. Yanev, C. Kastl, K. Zhang, A. W. Jansons, B. M. Crockett, K. M. Koskela, E. S. Barnard, E. Penzo, J. E. Hutchison, J. A. Robinson, L. Manna, N. J. Borys, P. J. Schuck, I. Kriegel, *Adv. Photonics Res.* **2021**, *2*, 2000151.
[55] A. Asaithambi, N. Kazemi Tofighi, N. Curreli, M. De Franco, A. Patra, N. Petrini, D. Baranov, L. Manna, F. D. Stasio, I. Kriegel, *Adv. Opt. Mater.* **2022**, *10*, 2200638.
[56] J. Schneider, D. W. Bahnemann, *J. Phys. Chem. Lett.* **2013**, *4*, 3479.
[57] K. Sathiyan, R. Bar-Ziv, V. Marks, D. Meyerstein, T. Zidki, *Chem. - Eur. J.* **2021**, *27*, 15936.
[58] B. Gürbulak, M. Şata, S. Dogan, S. Duman, A. Ashkhasi, E. F. Keskenler, *Phys. E* **2014**, *64*, 106.
[59] L. Najafi, S. Bellani, B. Martín-García, R. Oropesa-Nuñez, A. E. Del Rio Castillo, M. Prato, I. Moreels, F. Bonaccorso, *Chem. Mater.* **2017**, *29*, 5782.
[60] S. Bellani, A. Bartolotta, A. Agresti, G. Calogero, G. Grancini, A. Di Carlo, E. Kymakis, F. Bonaccorso, *Chem. Soc. Rev.* **2021**, *50*, 11870.
[61] L. Najafi, S. Bellani, M. I. Zappia, M. Serri, R. Oropesa-Nuñez, A. Bagheri, H. Beydaghi, R. Brescia, L. Pasquale, D. V Shinde, Y. Zuo, F. Drago, K. Mosina, Z. Sofer, L. Manna, F. Bonaccorso, *Nano Sel.* **2022**, *3*, 1069.
[62] L. Najafi, R. Oropesa-Nuñez, S. Bellani, B. Martín-García, L. Pasquale, M. Serri, F. Drago, J. Luxa, Z. Sofer, D. Sedmidubský, R. Brescia, S. Lauciello, M. I. Zappia, D. V. Shinde, L. Manna, F. Bonaccorso, *ACS Nano* **2022**, *16*, 351.
[63] A. E. Del Rio Castillo, V. Pellegrini, A. Ansaldo, F. Ricciardella, H. Sun, L. Marasco, J. Buha, Z. Dang, L. Gagliani, E. Lago, N. Curreli, S. Gentiluomo, F. Palazon, M. Prato, R. Oropesa-Nuñez, P. S. Toth, E. Mantero, M. Crugliano, A. Gamucci, A. Tomadin, M. Polini, F. Bonaccorso, *Mater. Horiz.* **2018**, *5*, 890.
[64] S. Bellani, E. Petroni, A. E. Del Rio Castillo, N. Curreli, B. Martín-García, R. Oropesa-Nuñez, M. Prato, F. Bonaccorso, *Adv. Funct. Mater.* **2019**, *29*, 1807659.
[65] M. A. Garakani, S. Bellani, V. Pellegrini, R. Oropesa-Nuñez, A. E. Del RioCastillo, S. Abouali, L. Najafi, B. Martín-García, A. Ansaldo, P. Bondavalli, C. Demirci, V. Romano, E. Mantero, L. Marasco, M. Prato, G. Bracciale, F. Bonaccorso, *Energy Storage Mater.* **2021**, *34*, 1.
[66] C. De Blasi, G. Micocci, S. Mongelli, A. Tepore, *J. Cryst. Growth* **1982**, *57*, 482.
[67] J. Camassel, P. Merle, H. Mathieu, A. Chevy, *Phys. Rev. B* **1978**, *17*, 4718.
[68] M. Brotons-Gisbert, D. Andres-Penares, J. Suh, F. Hidalgo, R. Abargues, P. J. Rodríguez-Cantó, A. Segura, A. Cros, G. Tobias, E. Canadell, P. Ordejón, J. Wu, J. P. Martínez-Pastor, J. F. Sánchez-Royo, *Nano Lett.* **2016**, *16*, 3221.
[69] G. W. Mudd, M. R. Molas, X. Chen, V. Zólyomi, K. Nogajewski, Z. R. Kudrynskyi, Z. D. Kovalyuk, G. Yusa, O. Makarovsky, L. Eaves, M. Potemski, V. I. Fal'ko, A. Patanè, *Sci. Rep.* **2016**, *6*, 39619.
[70] E. Petroni, E. Lago, S. Bellani, D. W. Boukhvalov, A. Politano, B. Gürbulak, S. Duman, M. Prato, S. Gentiluomo, R. Oropesa-Nuñez, J.-K. Panda, P. S. Toth, A. E. Del Rio Castillo, V. Pellegrini, F. Bonaccorso, *Small* **2018**, *14*, 1800749.
[71] L. I. Man, R. M. Imamov, S. A. Semiletov, *Kristallografiya* **1976**, *21*, 628.
[72] V. Zólyomi, N. D. Drummond, V. I. Fal'ko, *Phys. Rev. B* **2014**, *89*, 205416.
[73] D. K. Sang, H. Wang, M. Qiu, R. Cao, Z. Guo, J. Zhao, Y. Li, Q. Xiao, D. Fan, H. Zhang, *Nanomaterials* **2019**, *9*, 82.
[74] A. W. Jansons, J. E. Hutchison, *ACS Nano* **2016**, *10*, 6942.
[75] A. Agrawal, I. Kriegel, E. L. Runnerstrom, F. Scotognella, A. Llordes, D. J. Milliron, *ACS Photonics* **2018**, *5*, 2044.
[76] M. Ghini, N. Curreli, M. B. Lodi, N. Petrini, M. Wang, M. Prato, A. Fanti, L. Manna, I. Kriegel, *Nat. Commun.* **2022**, *13*, 537.
[77] I. Kriegel, F. Scotognella, L. Manna, *Phys. Rep.* **2017**, *674*, 1.
[78] A. W. Jansons, J. E. Hutchison, *ACS Nano* **2016**, *10*, 6942.
[79] J. A. Faucheaux, A. L. D. Stanton, P. K. Jain, *J. Phys. Chem. Lett.* **2014**, *5*, 976.
[80] X. Fan, W. Zheng, D. J. Singh, *Light: Sci. Appl.* **2014**, *3*, e179.
[81] M. Ghini, N. Curreli, A. Camellini, M. Wang, A. Asaithambi, I. Kriegel, *Nanoscale* **2021**, *13*, 8773.
[82] J. C. Scott, *J. Vac. Sci. Technol., A* **2003**, *21*, 521.
[83] R. A. Gilstrap, C. J. Capozzi, C. G. Carson, R. A. Gerhardt, C. J. Summers, *Adv. Mater.* **2008**, *20*, 4163.
[84] H. L. Zhuang, R. G. Hennig, *Chem. Mater.* **2013**, *25*, 3232.
[85] J. Aguirre, N. Medrano, B. Calvo, S. Celma, *Electron. Lett.* **2011**, *47*, 1172.
[86] M. Pourbaix, *Atlas of Electrochemical Equilibria in Aqueous Solutions*, National Association of Corrosion Engineers, Houston, TX **1974**, p. 436.
[87] V. Kumaravel, M. Imam, A. Badreldin, R. Chava, J. Do, M. Kang, A. Abdel-Wahab, *Catalysts* **2019**, *9*, 276.